Dielectric catastrophe at the Wigner-Mott transitions in a moiré superlattice

Yanhao Tang^{1,2*}, Jie Gu¹, Song Liu³, Kenji Watanabe⁴, Takashi Taniguchi⁴, James C. Hone³, Kin Fai Mak^{1,5,6*}, and Jie Shan^{1,5,6*}

¹School of Applied and Engineering Physics, Cornell University, Ithaca, NY, USA ²Interdisciplinary Center for Quantum Information, Zhejiang Province Key Laboratory of Quantum Technology, and Department of Physics, Zhejiang University, Hangzhou 310027, China

³Department of Mechanical Engineering, Columbia University, New York, NY, USA
⁴National Institute for Materials Science, 1-1 Namiki, 305-0044 Tsukuba, Japan
⁵Laboratory of Atomic and Solid State Physics, Cornell University, Ithaca, NY, USA
⁶Kavli Institute at Cornell for Nanoscale Science, Ithaca, NY, USA

These authors contributed equally: Yanhao Tang, Jie Gu *Email: yanhaotc@zju.edu.cn; kinfai.mak@cornell.edu; jie.shan@cornell.edu

The bandwidth-tuned Wigner-Mott transition, an interaction-driven transition from a generalized Wigner crystal to a Fermi liquid, is a fundamental and challenging problem in condensed-matter physics 1, 2. Because the transition is in general accompanied by both magnetic and charge-order instabilities ³⁻⁷, it remains unclear if a continuous Wigner-Mott transition exists. The emergence of semiconducting moiré materials with continuously tunable bandwidth provides an ideal platform to address this question 7-13. Here, we demonstrate bandwidth-tuned metal-insulator transitions at fixed fractional fillings of a MoSe₂/WS₂ moiré superlattice using the exciton sensing technique 14, 15. The bandwidth is controlled by an out-of-plane electric field. The dielectric response is probed optically with the 2s exciton in a remote WSe₂ sensor layer. The exciton spectral weight is negligible for the metallic state, consistent with a large negative dielectric constant. It continuously vanishes when the transition is approached from the insulating side, corresponding to a diverging dielectric constant or a 'dielectric catastrophe' driven by the critical charge dynamics near the transition ¹⁶⁻¹⁹. Our results support the scenario of continuous Wigner-Mott transitions in two-dimensional triangular lattices and stimulate future explorations of exotic quantum phases in their vicinities ^{3, 4, 6, 7, 20, 21}.

Metal-insulator transitions (MITs) accompanied by large electrical conductivity change are widely observed in condensed-matter systems $^{1, 2, 22-24}$. One particularly intriguing origin of charge localization and insulating phases is Coulomb repulsion between electrons 25 . The prototype model for interacting electrons in a lattice is the single-band Hubbard model with electronic bandwidth, W, and on-site Coulomb repulsion, U. The ground state of the electronic system for half band or full lattice filling is a Mott insulator in the strong interaction limit ($U \gg W$), and a Fermi liquid in the weak interaction limit ($U \ll W$). A MIT, the Mott transition, is expected near $U \sim W$ (Ref. 25). Similarly, if the electrons are localized by the extended Coulomb repulsion, V, instead of U, a Wigner-Mott insulator (or a generalized Wigner crystal) that spontaneously breaks the underlying

lattice space-group symmetries is formed at fractional lattice fillings $^{14, 26-28}$; a Wigner-Mott transition is expected near $V \sim W$ (Ref. $^{3-7}$). The evolution of a Mott or Wigner-Mott insulator into a metal as a function of the interaction strength remains a challenging theoretical problem $^{3-7, 23}$; it also raises an exciting opportunity for realizing exotic quantum phases near the transition if it is continuous $^{3, 4, 6, 7, 20, 21}$.

Experimentally, the interaction strength, or equivalently, the bandwidth can be tuned by applying isostatic or chemical pressure ¹. In almost all known materials, bandwidth-tuned MITs (the case of interest from now on) are driven first order 1 because the MITs are often accompanied by magnetic and structural phase transitions; it is difficult for the various kinds of transitions involving different order parameters to occur simultaneously without fine-tuning 1, 6, 20. The recent experimental breakthroughs in semiconducting transition metal dichalcogenide (TMD) moiré materials ^{14, 26, 29-31} have opened a new avenue to realize and study continuous bandwidth-tuned MITs 7-13. These materials form a two-dimensional (2D) triangular lattice that suppresses magnetic ordering due to geometric frustration. The electrons are trapped by the periodic moiré potential; they can tunnel between the moiré sites and interact with each other via both the on-site and extended Coulomb repulsions. This realizes the triangular-lattice extended Hubbard model ^{5, 8, 32, 33}. A variety of correlated insulating states are reported, including the Mott insulator ^{26, 29-31} at odd integer filling and Wigner-Mott insulators ^{14, 26-28, 34} at fractional fillings of the moiré superlattice. A continuous bandwidth-tuned Mott transition is also observed by electrical measurements 9, 10. However, the Wigner-Mott transition at fractional fillings remains elusive. In particular, it remains unclear if a continuous Wigner-Mott transition exists given the additional charge-ordering transition (besides possible magnetic transitions) near the MIT ^{3, 6}.

Here we report the observation of continuous bandwidth-tuned Wigner-Mott transitions in an angle-aligned MoSe₂/WS₂ heterobilayer by the exciton sensing technique ^{14, 15}. The heterobilayer forms a triangular moiré lattice with a lattice density of $\approx 1.9 \times 10^{12}$ cm⁻². It is encapsulated in hexagonal boron nitride (hBN) and gated by a top and bottom fewlayer graphite gate (Fig. 1a). The dual-gate structure enables independent tuning of the electron density in the moiré lattice ν (in units of the moiré density), and the out-of-plane electric field, E (> 0 for field pointing from the MoSe₂ to WS₂ layer). The MoSe₂/WS₂ heterobilayer has a type-I band alignment with both the conduction and valence band edges located in the MoSe₂ layer (Fig. 1b). The band offsets are $\Delta_c \sim 100$ meV for the conduction bands and $\Delta_{\nu} \sim 320$ meV for the valence bands from optical spectroscopy measurement (Methods). We tune the electronic bandwidth at a fixed doping density by the electric-field effect 9, 10. The out-of-plane electric field varies the moiré potential depth by controlling the band offset and the resonance interlayer hopping amplitude because spatial modulation in the interlayer hopping amplitude is one origin of the periodic moiré potential ^{8,9}. Because $\Delta_c < \Delta_v$, the electric-field effect on the conduction bandwidth is much larger; we focus on the case of electron doping.

The dielectric response of the moiré system, which can reflect the critical charge dynamics near continuous MITs ¹⁷⁻¹⁹, is probed by the exciton sensing technique. Recent studies show that the technique is highly sensitive to the insulating states ^{14, 15}. These

states perturb the electric field between the optically excited electrons and holes (excitons) in a charge neutral WSe₂ monolayer that is separated from the moiré superlattice by a bilayer hBN. The spacer thickness is smaller than the Bohr radius of the 2s and higher-energy exciton states. We probe the effective dielectric constant, ε , of the moiré heterobilayer by measuring the 2s exciton that has the largest spectral weight. Both the 2s exciton resonance energy and spectral weight, S, depend on ε (Ref. ³⁵). We analyze the spectral weight near the MITs (Methods). It is difficult to determine the exciton binding energy accurately since the band-to-band transitions are also renormalized and cannot be easily measured. Unless otherwise specified, all measurements are performed at 3.6 K; the corresponding thermal excitation energy is substantially lower than the characteristic energy scales (U, V and W) of the electronic system. Details on the device fabrication and optical measurements are provided in Methods.

Figure 1c shows the reflectance contrast spectrum of device 1 as a function of electron density ν in the strong interaction limit (U, V > W). The panels from left to right correspond to the moiré exciton of MoSe₂, the 2s exciton of the sensor layer, and the moiré exciton of WS₂, respectively. The moiré exciton spectra are consistent with a previous study ³⁶; the ground-state exciton in WS₂ remains robust for the entire doping range, indicating that the electrons are doped only into the MoSe₂ layer in the type-I heterostructure. A series of incompressible states emerge at integer multiples and specific fractions of the moiré density. They modulate the moiré exciton features, but more significantly, the sensor 2s exciton. At each incompressible state, the 2s exciton shows enhanced reflectance contrast or spectral weight (as well as spectral blueshift); it is consistent with small ε . The 2s exciton cannot be identified for the compressible states; it is merged into the band-to-band transitions ¹⁵. The quenching of the 2s exciton is consistent with large negative dielectric constant for a metallic phase.

The insulating states at even integers ($\nu = 2$ and 4) are the single-particle moiré band insulators. The odd integer states ($\nu = 1$ and 3) are the Mott or charge-transfer insulators ³². The fractional states (e.g. $\nu = 4/3$, 3/2, 5/3 etc.) are the Wigner-Mott insulators. Similar results are reported for a related WSe₂/WS₂ moiré superlattice ^{14, 26, 27, 30}. Generally, with increasing doping density the 2s exciton reflectance contrast decreases, and less fractional states can be identified. It reflects the decreasing importance of the Coulomb interaction at large doping densities. The second moiré band has a larger bandwidth compared to the first moiré band (Methods). We study the second moiré band with doping density $\nu = 2 - 4$, for which the field-tuned MITs are more easily achieved. For the same field range, a weak electric-field effect is observed for the first moiré band with $\nu = 0 - 2$ (Extended Data Fig. 1).

Figure 2 illustrates the evolution of the incompressible states probed by the sensor 2s exciton for v = 2 - 4 under increasing electric fields. To enhance the optical contrast of these states, we show the energy derivative of the reflectance contrast spectrum $dR/d\epsilon$. As electric field increases, the insulating states gradually "dissolve", first the band insulating state at v = 4, followed by the Wigner-Mott state at v = 7/3 and 8/3, and the Mott state at v = 3. The band insulating state at v = 2 remains robust. The order of disappearance of these states can differ slightly in different devices. The result for device

2 (Extended Data Fig. 2) shows that the fractional states disappear first, followed by the ν = 4 and 3 states; the latter two disappear at similar electric fields.

The above observation is consistent with the bandwidth-tuned MITs. As electric field increases (inducing larger Δ_c and shallower moiré potential), the moiré bandwidth W increases; this is the predominant effect since W is exponentially dependent on the moiré potential depth 8 . The disappearance of the $\nu=4$ state indicates closing of the band gap between the second and third moiré band as W increases. The vanishing $\nu=3$ and the fractional filling states reflect closing of the Mott charge gap and the Wigner-Mott charge gap when W becomes comparable to U and V, respectively. Because U>V, the fractional states disappear at smaller critical fields than the $\nu=3$ state in all devices examined in this study. On the other hand, the relative importance of the Mott gap and the band gap is sample dependent. A plausible origin is the twist angle and moiré density variations since these energies are generally charge-density dependent due to the strong correlation effects.

Next we investigate the bandwidth-tuned Mott and Wigner-Mott transitions systematically at fixed electron density of $\nu=3$ and 7/3, respectively. Figure 3a,b illustrate the sensor 2s exciton spectrum as a function of electric field. The 2s exciton resonance vanishes above a critical field, E_c . To determine the exciton spectral weight, we first normalize the reflectance contrast spectrum by that at a large field (e.g. 0.28 V/nm, above the critical field for $\nu=3$). In the metallic phase, the 2s exciton resonance is quenched (Fig. 2); the reflectance contrast spectrum is dominated by a broad hump corresponding to the band-to-band transitions ¹⁵; the spectrum is nearly identical to that at incommensurate fillings. Figure 3c shows the normalized spectrum at representative fields for $\nu=3$ (the result for $\nu=7/3$ is included in Extended Data Fig. 3). The integrated spectral weight (corresponding to the shaded area) is shown in Fig. 3d for $\nu=3$ and 7/3 as a function of electric field. As electric field or bandwidth increases, the spectral weight continuously decreases to zero. In addition, we do not observe any electric-field hysteresis within the experimental uncertainty. (The $\nu=3$ spectral weight decreases for negative electric fields because the MoSe₂ moiré bands are approaching the WS₂ bands.)

We infer the dielectric constant of the moiré heterobilayer from the measured sensor exciton spectral weight by modeling excitons in the 2D sensor layer using realistic device geometry (Extended Data Fig. 4). We numerically solve the electron-hole Schrodinger equation with screened Coulomb potential by the heterobilayer and the hBN substrate with dielectric constant ε and ε_{BN} , respectively. For $\varepsilon \gg \varepsilon_{BN}$, which holds for the insulting side near the transition, we obtain an empirical relation, $S \propto \varepsilon^{-0.7}$ (Methods). The field-dependence of ε inferred using the relation is included in Fig. 3d (black lines). Here ε is normalized by its value deep in the insulating phase, for which the 2s spectral weight plateaus. We also limit the electric-field range such that the signal-to-noise ratio of S stays above 1. We find that ε increases sharply towards the critical point for both $\nu = 3$ and 7/3; the electric-field dependence of ε is compatible with a power-law dependence, $\varepsilon \propto |E - E_c|^{-\gamma}$, with exponent $\gamma = 1.6 - 2.2$ for $\nu = 3$ and 1.2 - 1.8 for $\nu = 7/3$ (Extended Data Fig. 5). The dependence of ε on the metallic side cannot be extracted because of the vanished 2s exciton.

The diverging dielectric constant is consistent with the expectations for a continuous Mott/Wigner-Mott transition $^{16, 18}$. As the MIT critical point is approached from the insulating side, polarization fluctuations and the holon/doublon density proliferate, giving rise to a 'dielectric catastrophe' $\varepsilon \to \infty$ (Ref. 16); the charge gap $\Delta \propto \varepsilon^{-1/2}$ vanishes continuously 18 . The result reflects the critical charge dynamics near a continuous MIT and is not expected for a first order MIT. The continuous Mott transition at $\nu = 3$ agrees with recent transport studies of other TMD moiré materials $^{9, 10}$. The continuous Wigner-Mott transition at $\nu = 7/3$ is in qualitative agreement with theoretical analyses on the continuous bandwidth-tuned MIT at fractional lattice filling $^{3, 4, 6, 7}$. This transition can proceed through either a two-step process that involves an intermediate charge-density-wave metal $^{3, 6}$ or a one-step process that involves a deconfined quantum critical point $^{4, 6, 7}$. Our results are, however, unable to resolve the two scenarios. Additional Hall effect and optical conductivity measurements on the metallic side are required in future studies.

Finally, we examine the temperature dependence of these transitions. Figure 4a and 4b show the 2s exciton spectral weight as a function of electric field and temperature at $\nu =$ 3 and 7/3, respectively. The spectral weight is always negligible on the metallic side; it gradually decreases on the insulating side with increasing temperature because the thermally excited free carriers in the moiré heterobilayer screen the excitonic interaction in the sensor. The melting temperature is estimated to be ~ 65 K and 25 K, respectively, for the v = 3 and 7/3 states. We compare the electric-field dependence of S at 3.6 K and an elevated temperature for the two states in Fig. 4c and 4d. The spectral weight deep in the insulating phase is normalized to unity. At 3.6 K, the thermal excitation energy is small compared to the charge gap of both the Mott and Mott-Wigner insulators. Compared to the low-temperature behavior at 3.6 K, the MIT becomes a broadened metal-insulator crossover at high temperatures, a manifestation of critical point at lower temperatures. Our result thus suggests either a continuous Mott and Wigner-Mott transition with quantum critical point at zero temperature or weakly first-order transitions with critical point substantially below 3.6 K. The reduced dimensionality, the geometrically frustrated triangular lattice and the presence of disorders are known to favor continuous or weakly first-order transitions ^{6, 7, 20}. Above the critical point, these two scenarios are almost identical ³⁷; future experiments down to lower temperatures are required to distinguish them.

In conclusion, we have demonstrated bandwidth-tuned Wigner-Mott transitions at fixed band fillings of a Hubbard system based on semiconducting moiré materials. The transitions manifest a dielectric catastrophe when the critical point is approached from the insulating side. Our results present new opportunities to simulate Hubbard physics in the interesting regime of comparable Coulomb repulsion (U, V) and bandwidth (W), and to search for quantum spin liquids near the transitions $^{4, 6, 7, 20, 21}$.

Methods

Device fabrication. We fabricate dual-gate devices of a MoSe₂/WS₂ moiré heterobilayer with an integrated WSe₂ monolayer sensor using the reported dry transfer method ³⁸.

Briefly, atomically thin flakes are first exfoliated from bulk crystals onto Si substrates and then stacked using a polymer stamp to form the desired heterostructure. Monolayer MoSe₂ and WS₂ flakes are angle aligned with a precision of about 0.5°. The orientation and relative alignment of these crystals are determined from the angle-resolved optical second harmonic measurement ³⁰. The WSe₂ sensor is separated from the moiré heterobilayer by a bilayer hBN. The TMD moiré heterobilayer and the sensor are grounded through few-layer graphite electrodes. The entire heterostructure is gated by hBN gate dielectrics (≈ 25 nm) and few-layer graphite gates on both sides.

Optical reflectance contrast measurements and analysis. Details of the reflectance contrast measurement are reported in the literature ^{14, 30}. Briefly, broadband white light from a tungsten-halogen lamp is focused under normal incidence to a diffraction-limited spot on the device by a high-numerical-aperture objective. The device is mounted in a closed-cycle cryostat with base temperature of 3.6 K (attoDry 1000). The reflected light is collected by the same objective and detected by a spectrometer with a liquid-nitrogen cooled charge-coupled device (CCD). The reflectance contrast spectrum $R \equiv (I' - I)/I$ is obtained by comparing the reflected light spectrum from the sample (I') with a featureless background spectrum (I).

To analyze the 2s exciton spectral weight, we integrate the normalized reflectance contrast over a spectral window of 5 nm centered at the resonance. Specifically, we define a straight line that connects the end points of the integration window as a baseline, and integrate the area above it (Fig. 3c). To verify the reliability of the procedure, we have varied the size of the integration window; the process does not affect the electric field dependence of the 2s spectral weight.

Band alignment of the MoSe₂/WS₂ heterobilayer. We determine the band alignment of the MoSe₂/WS₂ heterobilayer by examining a sample with large twist angle to avoid the moiré effect for simplicity. The reflectance contrast spectrum is measured as a function of doping density under zero applied electric field. Extended Data Fig. 6a and b show the fundamental exciton resonance in monolayer MoSe₂ and WS₂, respectively. The neutral exciton feature turns into the charged exciton (or polaron) feature in MoSe₂ with both electron and hole doping; the optical response of the WS₂ layer remains largely unperturbed. Charges are therefore introduced only into the MoSe₂ layer upon both electron and hole doping; the MoSe₂/WS₂ heterobilayer has a type-I band alignment.

We determine the band offsets by measuring the electric-field (E) dependence of the reflectance contrast spectrum. We choose a fixed electron doping density ($\approx 3.7 \times 10^{12}$ cm⁻²); the chemical potential is slightly above the conduction band edge of MoSe₂. As E increases in the WS₂ to MoSe₂ direction (E < 0), the charged exciton feature in MoSe₂ changes to the neutral exciton above $E_0 \approx -0.33$ V/nm (Extended Data Fig. 6c); at the same time, the neutral exciton feature in WS₂ turns into the charged exciton (Extended Data Fig. 6d). The spectral changes correspond to the onset of charge transfer from MoSe₂ to WS₂ when the two conduction bands become nearly degenerate. Using the reported interlayer dipole moment in the MoSe₂/WS₂ heterobilayer ³⁶, $d \approx 0.3$ e·nm, we estimate the conduction band offset to be $\Delta_C = d \cdot E_0 \approx 0.1$ eV. The valence band offset

can be evaluated as $\Delta_V \approx E_g^W - E_g^{Mo} - \Delta_C \approx 0.32$ eV, where $E_g^W \approx 2.04$ eV and $E_g^{Mo} \approx 1.62$ eV are the optical gaps of monolayer MoSe₂ and WS₂, respectively. Extended Data Fig. 6e illustrates the inferred band alignment.

Estimate of the bandwidth. We estimate the first moiré conduction bandwidth, $W_0 \sim \frac{\hbar^2}{ma_M^2} \sim 5$ - 10 meV (corresponding to a temperature scale ~ 60 - 120 K), from the moiré period a_M . Here \hbar and m denote the Planck's constant and the conduction band mass of monolayer MoSe₂, respectively ($m \approx 0.56 \, m_0$ in terms of the free electron mass m_0) ³⁹. The combined width of the first two moiré bands is $4W_0$; the second moiré bandwidth is about $3W_0$ (~ 180 - 360 K). These values are substantially smaller than $\Delta_C \approx 0.1 \, \text{eV}$ ($\sim 1200 \, \text{K}$). We focus on the second moiré conduction band with larger bandwidth so that the sample temperature is small compared to the bandwidth and the bandwidth-tuned MITs are easier to achieve. The electrons reside in the MoSe₂ layer for all electric fields and doping densities in this study.

Modeling the 2s exciton of the sensor layer. Quantitative estimate of the effective dielectric constant of the moiré heterobilayer is obtained by modeling the sensor 2s exciton (Extended Data Fig. 4). We solve the Schrödinger equation, $H\Psi_{ns}(\rho) = E_{ns}\Psi_{ns}(\rho)$, for the energy (E_{ns}) and wavefunction $(\Psi_{ns}(\rho))$ of the ns (n=1,2,...) exciton state using the finite difference method 40 . For radially symmetric ns excitons confined in the 2D sensor plane, the Hamiltonian is given by $H = -\frac{\hbar^2}{2m_R} \left(\partial_\rho^2 + \frac{1}{\rho} \partial_\rho \right) + V(\rho)$, where ρ is the distance between the electron and hole, m_R ($\approx 0.2 \, m_0$ [Ref. 41]) is the reduced mass of the exciton, and $V(\rho)$ is the electrostatic potential between the electron and hole. We model $V(\rho)$ using the device geometry shown in Extended Data Fig. 4a. The thickness of the sensor layer, which is substantially smaller than the 2s exciton Bohr radius (~ 5 nm), is ignored; the thickness of the hBN spacer and the moiré heterobilayer are d_1 and d_2 , respectively; the hBN gate dielectric is assumed to be infinitely thick. The latter is a good approximation when the exciton Bohr radius does not exceed substantially the hBN thickness and screening by the graphite gates is negligible. We express the potential as follows 42

$$V(\rho) = -\frac{e^2}{4\pi\varepsilon_0\varepsilon_{BN}} \left[-\frac{1}{\rho} + \sum_{j=0}^{\infty} \beta^{2j+1} \left(\frac{1}{\sqrt{\rho^2 + 4(d_1 + jd_2)^2}} - \frac{1}{\sqrt{\rho^2 + 4(d_1 + (j+1)d_2)^2}} \right) \right]. (1)$$

Here ε_0 is the vacuum permittivity; $\beta = (\varepsilon - \varepsilon_{BN})/(\varepsilon + \varepsilon_{BN})$ is given by the dielectric constant of hBN ($\varepsilon_{BN} = 4.5$ [Ref. ¹⁴]) and the heterobilayer (ε); we take $d_1 = 0.9$ nm for a 2L-hBN spacer and $d_2 = 0.6$ nm for electrons residing in the MoSe₂ layer of the moiré. We assume ε to be a real value for the insulating states for simplicity. For ρ larger than the 1s exciton Bohr radius (< 2 nm), the potential $V(\rho)$ in Eqn. (1) is a good approximation for the more accurate Rytova-Keldysh potential for 2D excitons ^{40, 43, 44} (Extended Data Fig. 7). Since we focus on 2s sensing in this study, Eqn. (1) is sufficient; we can ignore the finite sensor thickness.

Extended Data Fig. 4b and 4c illustrate the spatial distribution of potential $V(\rho)$ and wavefunction $\Psi_{2s}(\rho)$ of the 2s exciton for several values of $\varepsilon/\varepsilon_{BN}$. The 2s exciton radius

 $r_{2s} \ (= \sqrt{\langle \Psi_{2s} | \rho^2 | \Psi_{2s} \rangle})$ and binding energy E_{2s} as a function of $\varepsilon / \varepsilon_{BN}$ are shown in Extended Data Fig. 4d and 4e, respectively. For $\varepsilon/\varepsilon_{BN}=2$, screening by the heterobilayer is negligible; we have $V(\rho) \approx -\frac{e^2}{4\pi\varepsilon_0\varepsilon_{B}\rho}$ and $r_{2s} \approx 4.7$ nm. The latter agrees well with the reported value of $r_{2s} \approx 6.6$ nm for monolayer WSe₂ embedded in hBN ⁴⁰. As $\varepsilon/\varepsilon_{BN}$ increases, $V(\rho)$ is suppressed and $\Psi_{2s}(\rho)$ is flattened; r_{2s} increases and E_{2s} decreases. For $\varepsilon/\varepsilon_{BN}=10^4$, r_{2s} exceeds 50 nm. We limit the range of $\varepsilon/\varepsilon_{BN}$ to $<10^4$ (so that the correction from the gate screening effect remains small) and perform a power-law analysis of E_{2s} . The binding energy is well described by $\sim (\frac{\varepsilon}{\varepsilon_{BN}})^{-0.7}$ for $\frac{\varepsilon}{\varepsilon_{BN}} > 10$ (solid line in Extended Data Fig. 4e). The exciton spectral weight is expected to follow the same scaling law on the dielectric constant since both the exciton spectral weight and binding energy scale quadratically with inverse of the exciton radius, which represents the total number of electronic states constituting the exciton 45 (Extended Data Fig. 4f shows $E_{2s} \sim (r_{2s})^{-2}$ for the entire range of dielectric constant). We examine the result for several hBN space thicknesses. The power-law exponent of -0.7 remains a good approximation as long as the spacer thickness is much smaller than the 2s exciton radius. In the main text, we use the power-law dependence to extract the evolution of the dielectric constant on the out-of-plane electric field from the experimental spectral weight.

References

- 1. Imada, M., Fujimori, A. & Tokura, Y. Metal-insulator transitions. *Reviews of Modern Physics* **70**, 1039-1263 (1998).
- 2. Dobrosavljevic, V., Trivedi, N. & Valles Jr, J. M. Conductor insulator quantum phase transitions (Oxford University Press, 2012).
- 3. Camjayi, A., Haule, K., Dobrosavljević, V. & Kotliar, G. Coulomb correlations and the Wigner–Mott transition. *Nature Physics* **4**, 932-935 (2008).
- 4. Chen, G., Kee, H.-Y. & Kim, Y.B. Fractionalized Charge Excitations in a Spin Liquid on Partially Filled Pyrochlore Lattices. *Physical Review Letters* **113**, 197202 (2014).
- 5. Pan, H., Wu, F. & Das Sarma, S. Quantum phase diagram of a Moir\'e-Hubbard model. *Physical Review B* **102**, 201104 (2020).
- 6. Seth Musser, T.S., Debanjan Chowdhury. Theory of a Continuous Bandwidthtuned Wigner-Mott Transition. *arXiv:2111.09894* (2021).
- 7. Yichen Xu, X.-C.W., Zhu-Xi Luo, Meng-Xing Ye, Chao-Ming Jian, Cenke Xu. Metal-Insulator Transition with Charge Fractionalization. *arXiv:2106.14910* (2021).
- 8. Wu, F., Lovorn, T., Tutuc, E. & MacDonald, A.H. Hubbard Model Physics in Transition Metal Dichalcogenide Moir\'e Bands. *Physical Review Letters* **121**, 026402 (2018).
- 9. Li, T. et al. Continuous Mott transition in semiconductor moiré superlattices. *Nature* **597**, 350-354 (2021).
- 10. Ghiotto, A. et al. Quantum criticality in twisted transition metal dichalcogenides. *Nature* **597**, 345-349 (2021).

- 11. Morales-Durán, N., MacDonald, A.H. & Potasz, P. Metal-insulator transition in transition metal dichalcogenide heterobilayer moir\'e superlattices. *Physical Review B* **103**, L241110 (2021).
- 12. Pan, H. & Das Sarma, S. Interaction-Driven Filling-Induced Metal-Insulator Transitions in 2D Moir\'e Lattices. *Physical Review Letters* **127**, 096802 (2021).
- 13. Jiawei Zang, J.W., Jennifer Cano, Antoine Georges, Andrew J. Millis. Dynamical mean field theory of moiré bilayer transition metal dichalcogenides: phase diagram, resistivity, and quantum criticality. *arXiv:2112.03080* (2021).
- 14. Xu, Y. et al. Correlated insulating states at fractional fillings of moiré superlattices. *Nature* **587**, 214-218 (2020).
- 15. Xu, Y. et al. Creation of moiré bands in a monolayer semiconductor by spatially periodic dielectric screening. *Nature Materials* **20**, 645-649 (2021).
- 16. Mott, N.F. Metal-insulator transition (Taylor & Francis, London, 1974).
- 17. Rosenbaum, T.F. et al. Metal-insulator transition in a doped semiconductor. *Physical Review B* **27**, 7509-7523 (1983).
- 18. Aebischer, C., Baeriswyl, D. & Noack, R.M. Dielectric Catastrophe at the Mott Transition. *Physical Review Letters* **86**, 468-471 (2001).
- 19. Rösslhuber, R. et al. Phase coexistence at the first-order Mott transition revealed by pressure-dependent dielectric spectroscopy of κ–(BEDT–TTF)2–Cu2(CN)3. *Physical Review B* **103**, 125111 (2021).
- 20. Senthil, T. Theory of a continuous Mott transition in two dimensions. *Physical Review B* **78**, 045109 (2008).
- 21. Szasz, A., Motruk, J., Zaletel, M.P. & Moore, J.E. Chiral Spin Liquid Phase of the Triangular Lattice Hubbard Model: A Density Matrix Renormalization Group Study. *Physical Review X* **10**, 021042 (2020).
- 22. Georges, A., Kotliar, G., Krauth, W. & Rozenberg, M.J. Dynamical mean-field theory of strongly correlated fermion systems and the limit of infinite dimensions. *Reviews of Modern Physics* **68**, 13-125 (1996).
- 23. Spivak, B., Kravchenko, S.V., Kivelson, S.A. & Gao, X.P.A. Colloquium: Transport in strongly correlated two dimensional electron fluids. *Reviews of Modern Physics* **82**, 1743-1766 (2010).
- 24. Abrahams, E., Kravchenko, S.V. & Sarachik, M.P. Metallic behavior and related phenomena in two dimensions. *Reviews of Modern Physics* **73**, 251-266 (2001).
- 25. Mott, N.F. Metal-Insulator Transition. *Reviews of Modern Physics* **40**, 677-683 (1968).
- 26. Regan, E.C. et al. Mott and generalized Wigner crystal states in WSe2/WS2 moiré superlattices. *Nature* **579**, 359-363 (2020).
- 27. Huang, X. et al. Correlated insulating states at fractional fillings of the WS2/WSe2 moiré lattice. *Nature Physics* 17, 715-719 (2021).
- 28. Li, H. et al. Imaging two-dimensional generalized Wigner crystals. *Nature* **597**, 650-654 (2021).
- 29. Shimazaki, Y. et al. Strongly correlated electrons and hybrid excitons in a moiré heterostructure. *Nature* **580**, 472-477 (2020).
- 30. Tang, Y. et al. Simulation of Hubbard model physics in WSe2/WS2 moiré superlattices. *Nature* **579**, 353-358 (2020).

- Wang, L. et al. Correlated electronic phases in twisted bilayer transition metal dichalcogenides. *Nature Materials* **19**, 861-866 (2020).
- Zhang, Y., Yuan, N.F.Q. & Fu, L. Moir'e quantum chemistry: Charge transfer in transition metal dichalcogenide superlattices. *Physical Review B* **102**, 201115 (2020).
- 33. Slagle, K. & Fu, L. Charge transfer excitations, pair density waves, and superconductivity in moir\'e materials. *Physical Review B* **102**, 235423 (2020).
- Jin, C. et al. Stripe phases in WSe2/WS2 moiré superlattices. *Nature Materials* **20**, 940-944 (2021).
- 35. Raja, A. et al. Coulomb engineering of the bandgap and excitons in two-dimensional materials. *Nature Communications* **8**, 15251 (2017).
- 36. Tang, Y. et al. Tuning layer-hybridized moiré excitons by the quantum-confined Stark effect. *Nature Nanotechnology* **16**, 52-57 (2021).
- 37. Vučičević, J., Terletska, H., Tanasković, D. & Dobrosavljević, V. Finite-temperature crossover and the quantum Widom line near the Mott transition. *Physical Review B* **88**, 075143 (2013).
- 38. Wang, L. et al. One-Dimensional Electrical Contact to a Two-Dimensional Material. *Science* **342**, 614-617 (2013).
- 39. Kormányos, A. et al. k · p theory for two-dimensional transition metal dichalcogenide semiconductors. *2D Materials* **2**, 022001 (2015).
- 40. Stier, A.V. et al. Magnetooptics of Exciton Rydberg States in a Monolayer Semiconductor. *Physical Review Letters* **120**, 057405 (2018).
- 41. Mak, K.F. & Shan, J. Photonics and optoelectronics of 2D semiconductor transition metal dichalcogenides. *Nature Photonics* **10**, 216-226 (2016).
- 42. Chen, T. & Bowler, N. Analysis of a concentric coplanar capacitive sensor for nondestructive evaluation of multi-layered dielectric structures. *IEEE Transactions on Dielectrics and Electrical Insulation* **17**, 1307-1318 (2010).
- Chernikov, A. et al. Exciton Binding Energy and Nonhydrogenic Rydberg Series in Monolayer \${\mathrm{WS}}_{2}\$. *Physical Review Letters* **113**, 076802 (2014).
- 44. He, K. et al. Tightly Bound Excitons in Monolayer ${\text{WSe}}_{2}$. *Physical Review Letters* **113**, 026803 (2014).
- 45. Hanamura, E., Nagaosa, N., Kumagai, M. & Takagahara, T. Quantum wells with enhanced exciton effects and optical non-linearity. *Materials Science and Engineering: B* 1, 255-258 (1988).

Figures

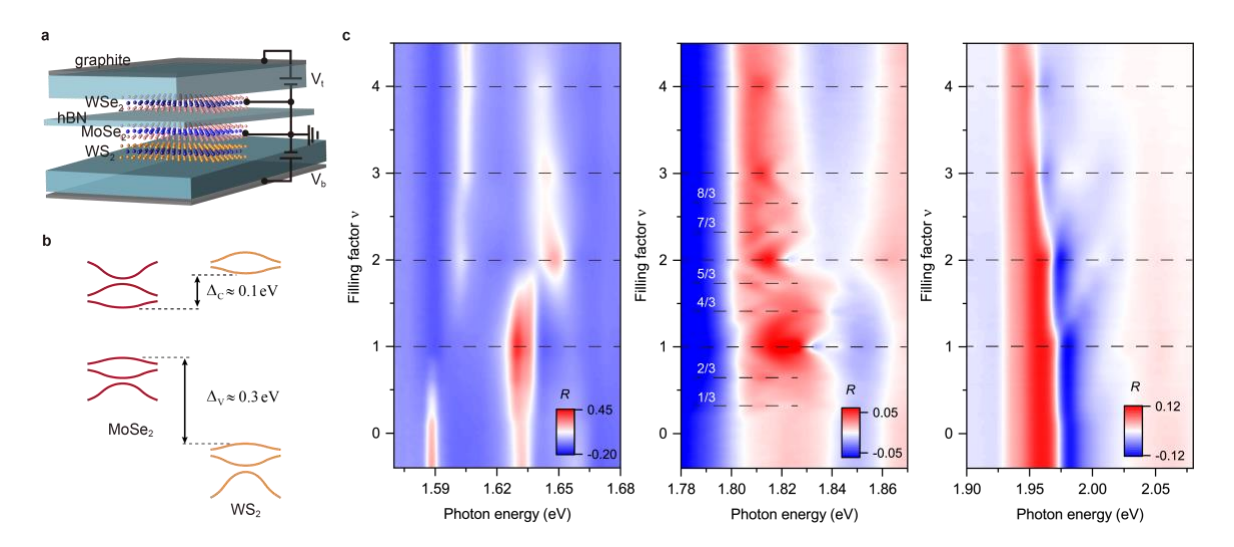


Figure 1 | Correlated insulating states in MoSe₂/WS₂ moiré heterobilayers. a, Schematic illustration of a dual-gated MoSe₂/WS₂ moiré heterobilayer with an integrated WSe₂ monolayer sensor separated by bilayer hBN. Voltage V_t and V_b are applied to the top and bottom hBN-graphite gates, respectively. Both the moiré heterobilayer and the sensor are grounded. b, MoSe₂/WS₂ moiré heterobilayer has a type-I band alignment with $\Delta_c \approx 0.3$ eV. c, Reflectance contrast spectrum of device 1 as a function of electron doping density ν (in units of the moiré density). Full lattice fillings are denoted by dashed lines. The panels from left to right correspond to the moiré exciton of MoSe₂, the sensor 2s exciton, and the moiré exciton of WS₂, respectively. The incompressible states are identified by the enhanced reflectance contrast of the 2s exciton.

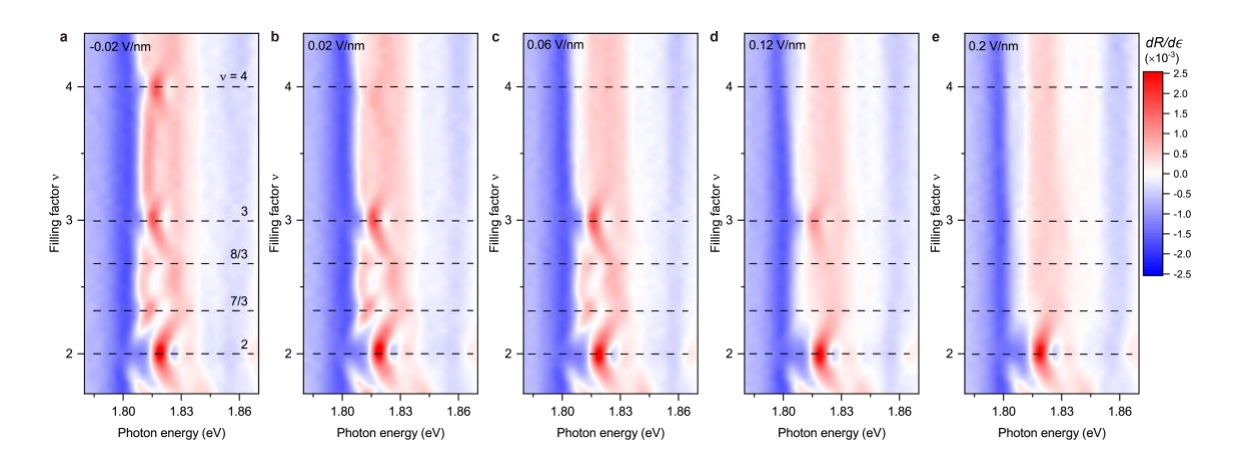


Figure 2 | Electric-field-tuned MITs. a-e, The energy-derivative of the reflectance contrast spectrum $(dR/d\epsilon)$ of the sensor 2s exciton as a function of electron filling factor $(\nu=2$ - 4) under out-of-plane electric field of -0.02 V/nm (a), 0.02 V/nm (b), 0.06 V/nm (c), 0.12 V/nm (d) and 0.2 V/nm (e). The incompressible states at E=-0.02 V/nm manifest enhanced reflectance contrast and are labeled by the dashed black lines. They gradually dissolve as electric field increases.

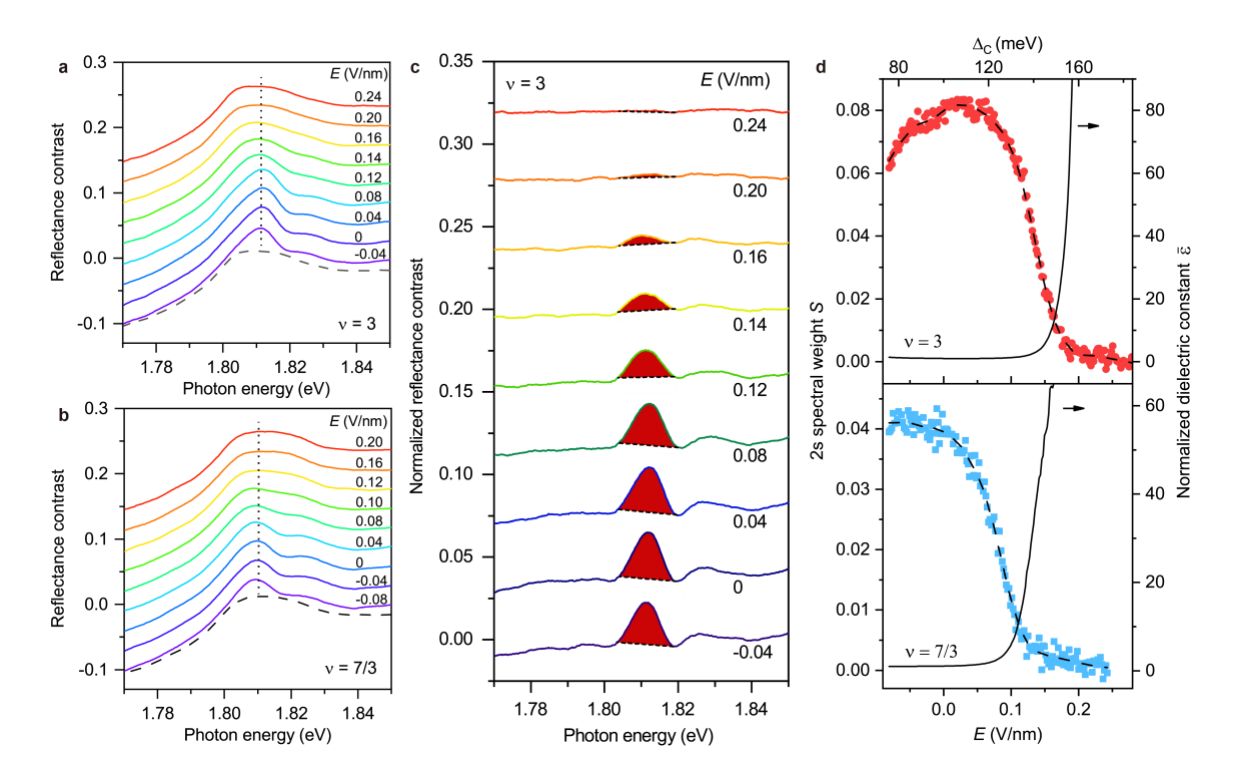


Figure 3 | Dielectric catastrophe near the Mott and Wigner transitions. a, b, Reflectance contrast spectrum of the sensor 2s exciton under varying electric fields at fixed electron filling factor of $\nu = 3$ (a) and 7/3 (b). The spectra are vertically displaced by a constant 0.03. The dashed lines represent the reflectance contrast spectra at high electric fields (0.28 V/nm and 0.24 V/nm for $\nu = 3$ and 7/3, respectively), in which the broad humps correspond to the band-to-band transitions. The vertical dotted lines denote the 2s exciton peak. c, Reflectance contrast spectrum at $\nu = 3$, normalized by that at 0.28 V/nm (in the metallic phase), at representative electric fields. The spectral weight S is extracted by integrating the shaded area. d, The extracted 2s spectral weight S (symbols) as a function of electric field (bottom axis) and Δ_c (top axis) for $\nu = 3$ (upper panel) and ν = 7/3 (lower panel). The band offset Δ_c is calculated using the applied electric field as described in Methods. The dashed lines are the smoothed data using the Savitzky-Golay algorithm with a window of 80 mV/nm. The solid lines are the dielectric constant $\bar{\varepsilon}$ of the moiré heterobilayer (right axis) that is normalized to unity at 0.02 V/nm and -0.08 V/nm (upper and lower panel, deep in the insulating phase). It is obtained from the dashed lines using the empirical relation, $S \propto \varepsilon^{-0.7}$ (Methods).

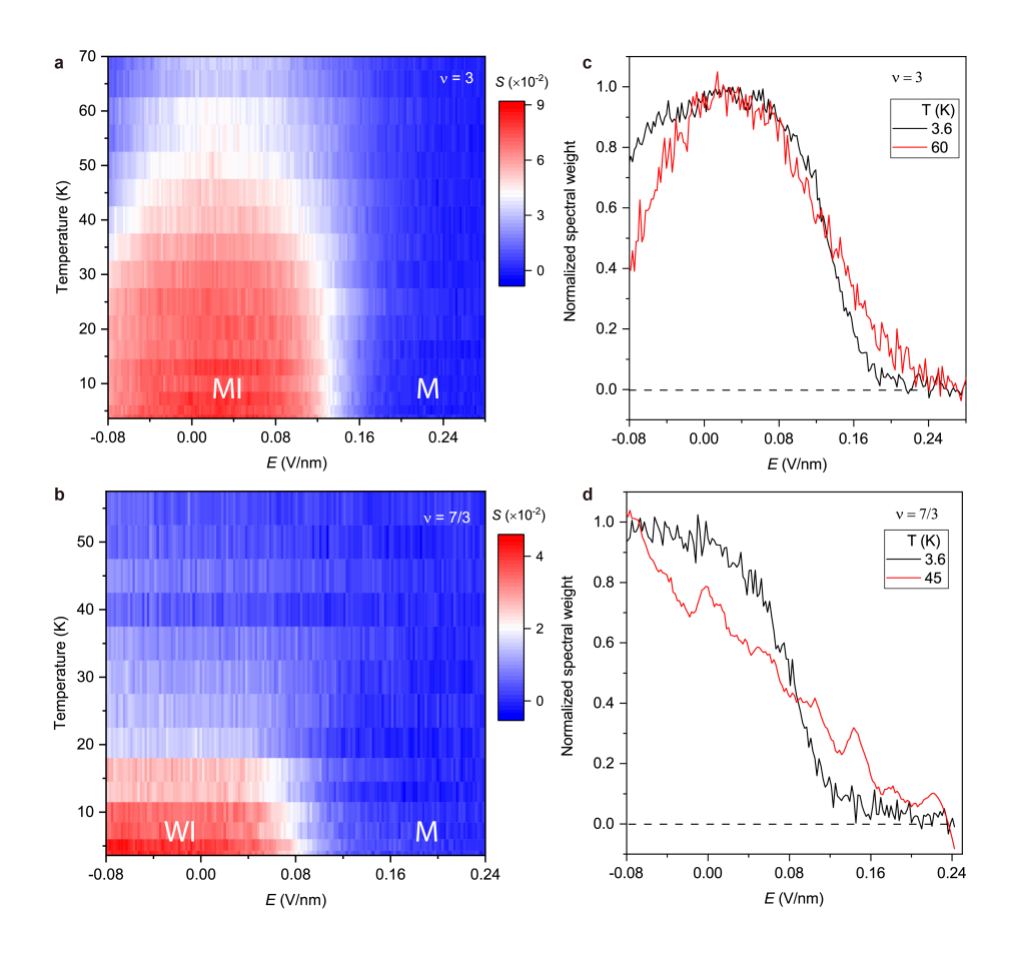
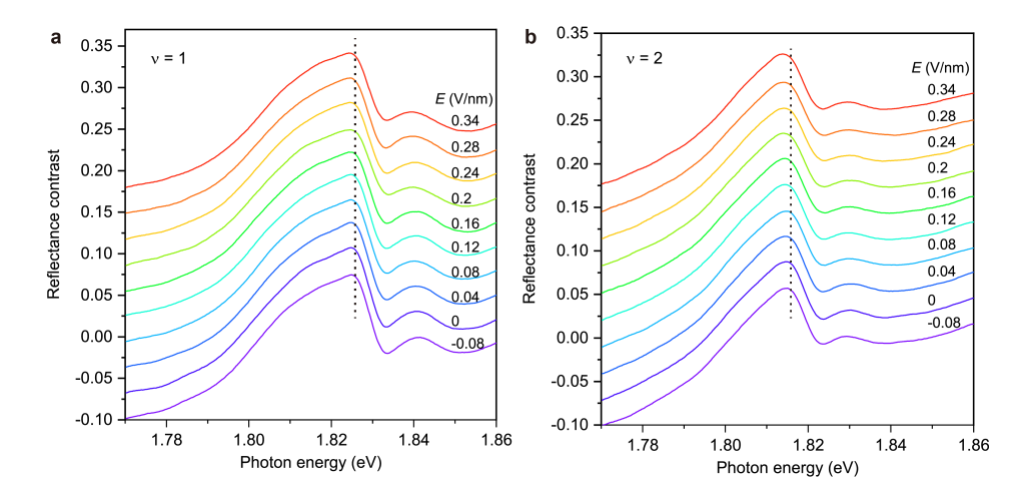
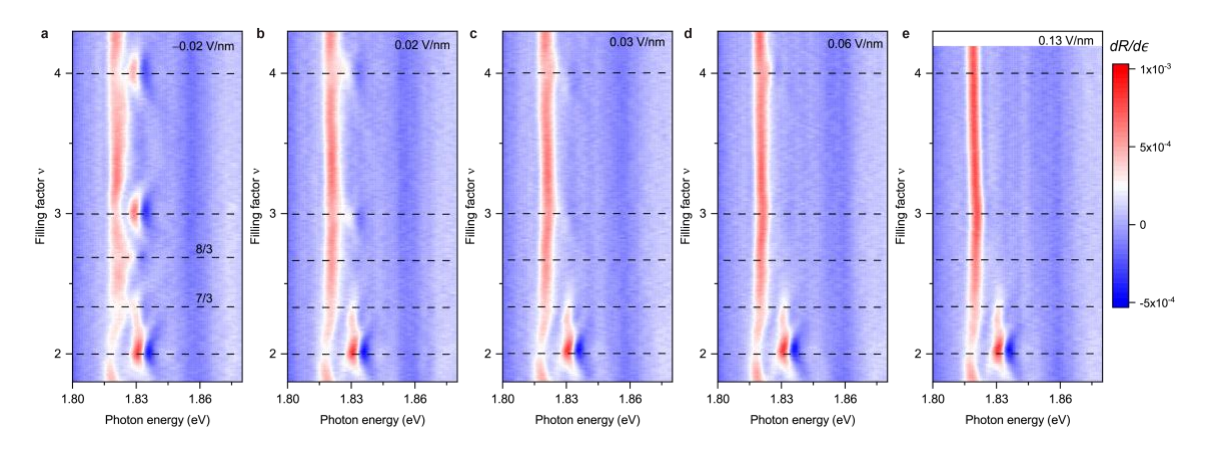


Figure 4 | **Temperature dependence. a, b,** Contour plot of the sensor 2s spectral weight as a function of temperature and electric field for $\nu = 3$ (a) and $\nu = 7/3$ (b). MI, WI, and M represent, respectively, the Mott insulator, Mott-Wigner insulator, and metal. Regions with enhanced spectral weight (red) correspond to the incompressible states (MI and WI); regions with negligible spectral weight (blue) correspond to the compressible states (metal). **c**, **d**, Electric-field dependence of the 2s spectral weight at selected temperatures for $\nu = 3$ (c) and $\nu = 7/3$ (d). The spectral weight maximum is normalized to unity. The metal-insulator crossover is broadened at high temperatures.

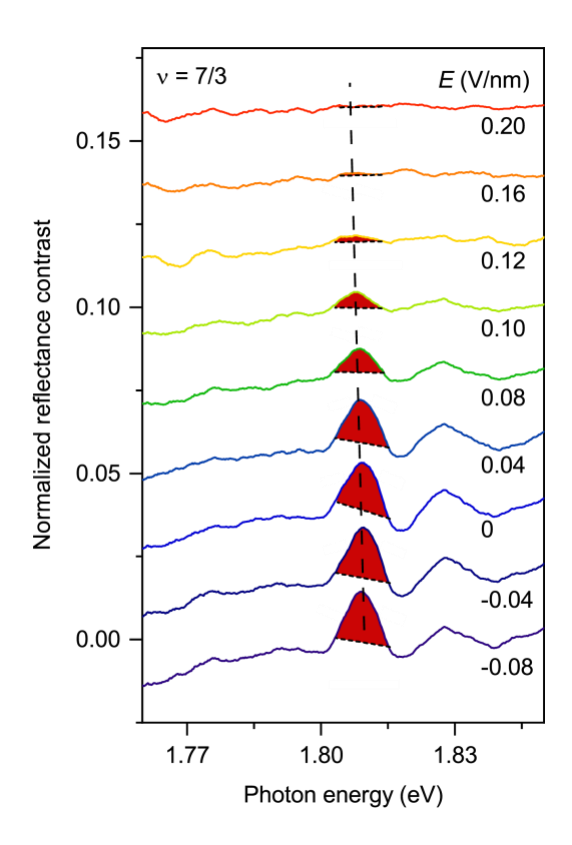
Extended data figures



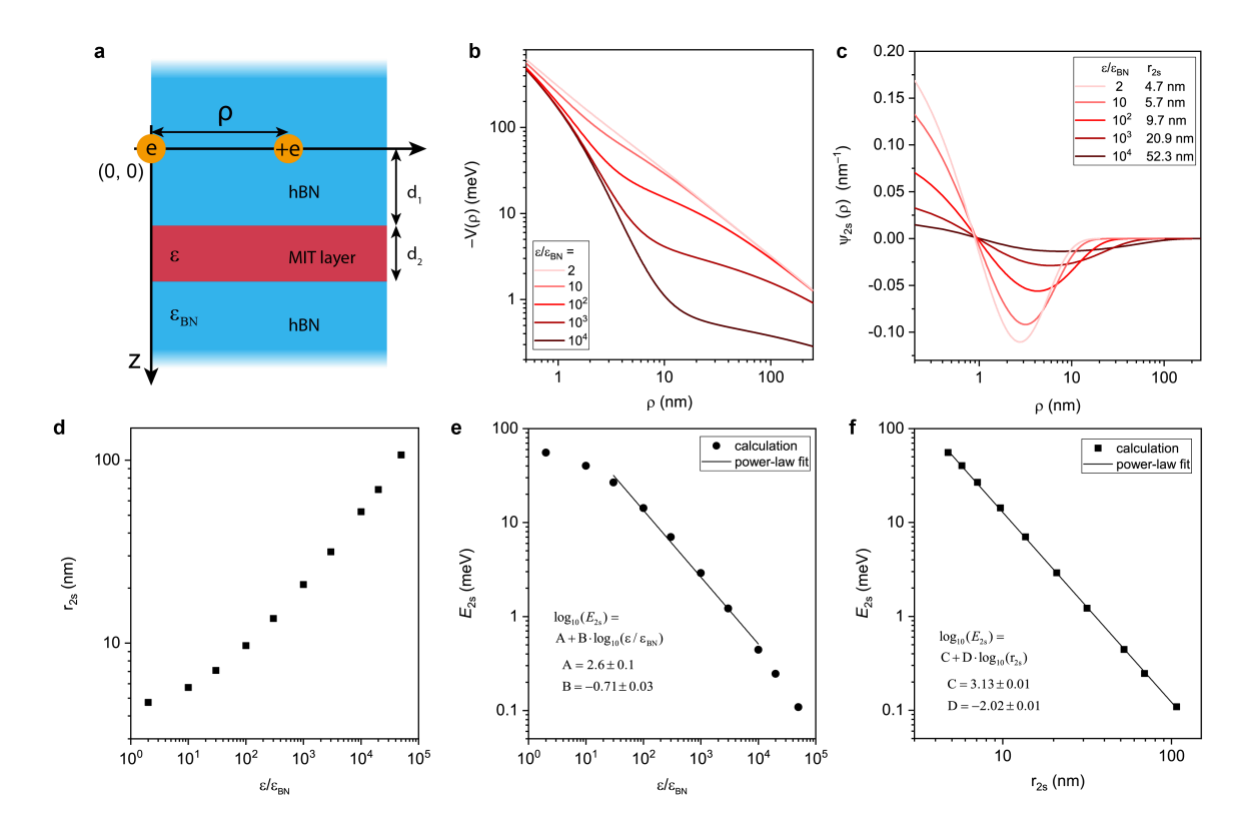
Extended Data Figure 1 | Electric-field dependence at $\nu=1$ and $\nu=2$. The reflectance contrast spectrum near the sensor 2s exciton under representative electric fields at $\nu=1$ (a) and $\nu=2$ (b). The spectra are vertically displaced by a constant 0.03 for clarity. The vertical dotted lines trace the 2s exciton peak. Negligible electric-field dependence is observed.



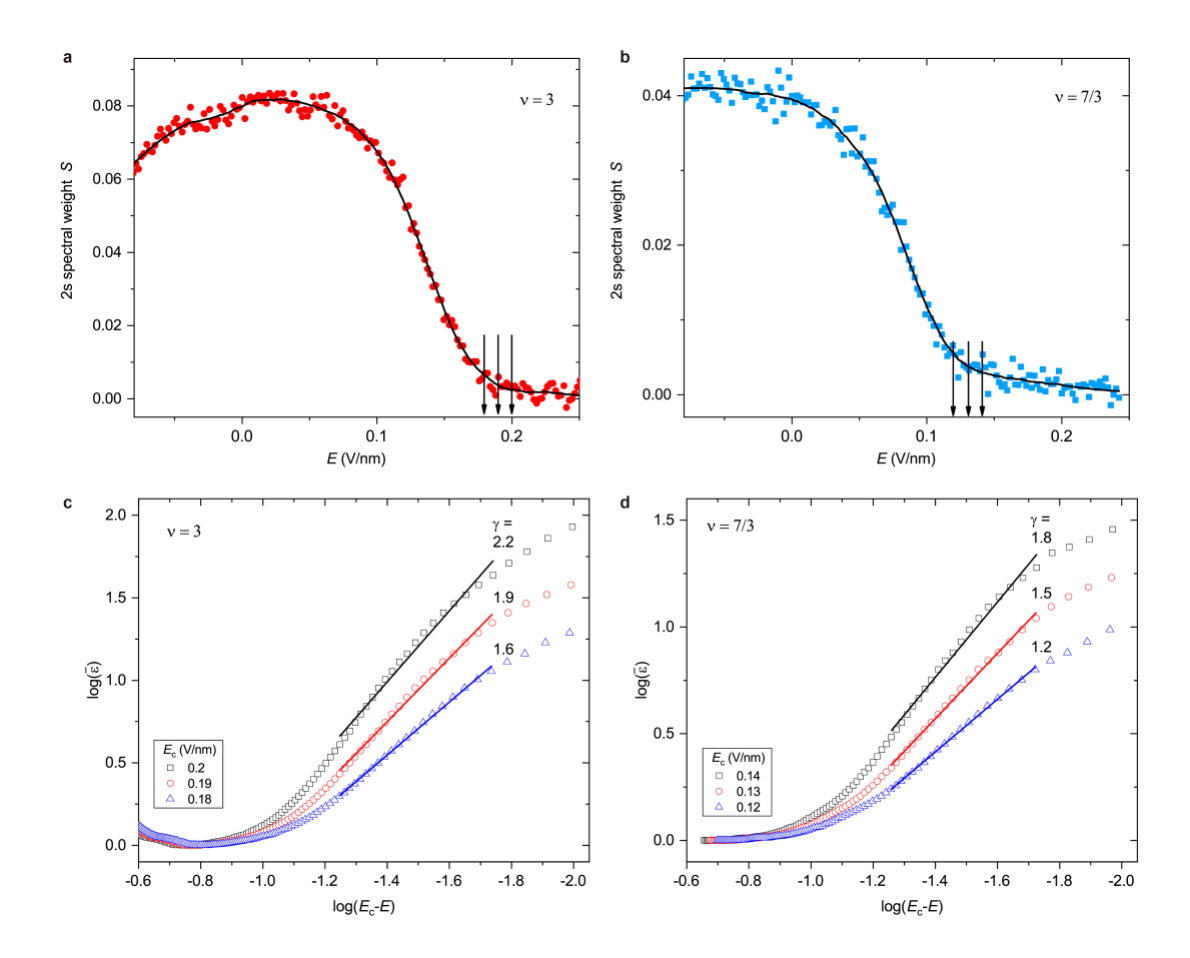
Extended Data Figure 2 | Electric-field tuned MITs in device 2. a-e, The energy-derivative of the reflectance contrast spectrum $(dR/d\epsilon)$ of the sensor 2s exciton as a function of electron filling factor ($\nu=2$ - 4) at electric field E ranging from -0.02 V/nm to 0.13 V/nm. The incompressible states at E=-0.02 V/nm are labeled by the dashed black lines. They gradually dissolve as electric field increases. The $\nu=4$ and $\nu=3$ insulating states disappear at a similar electric field in this device.



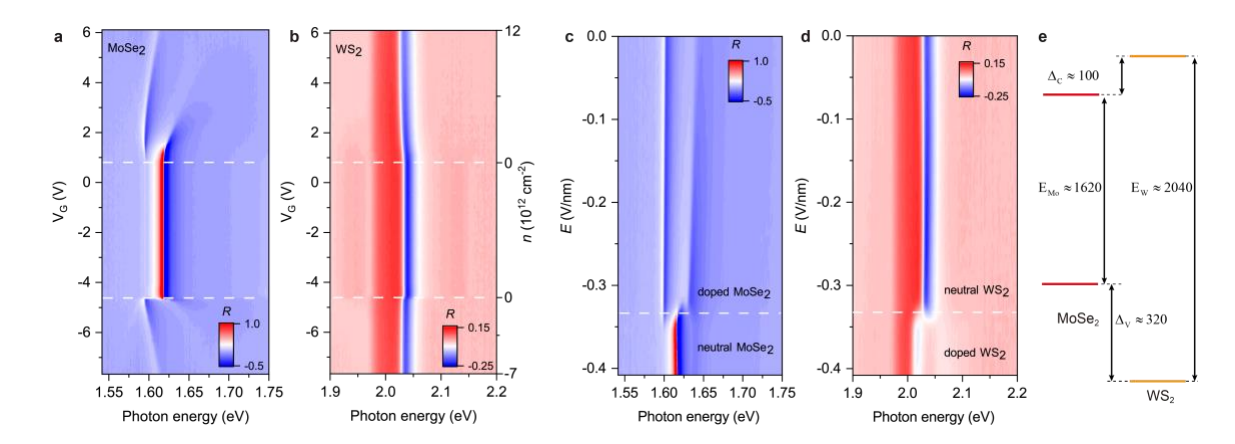
Extended Data Figure 3 | Normalized reflectance contrast spectra of the sensor 2s exciton at representative electric fields at $\nu=7/3$. The reflectance contrast spectra are normalized to that at 0.24 V/nm, under which no incompressible states can be identified. The 2s exciton oscillator strength (shaded area) decreases to zero at large electric fields. The spectra are vertically displaced by a constant 0.02. The dashed line traces the 2s exciton peak.



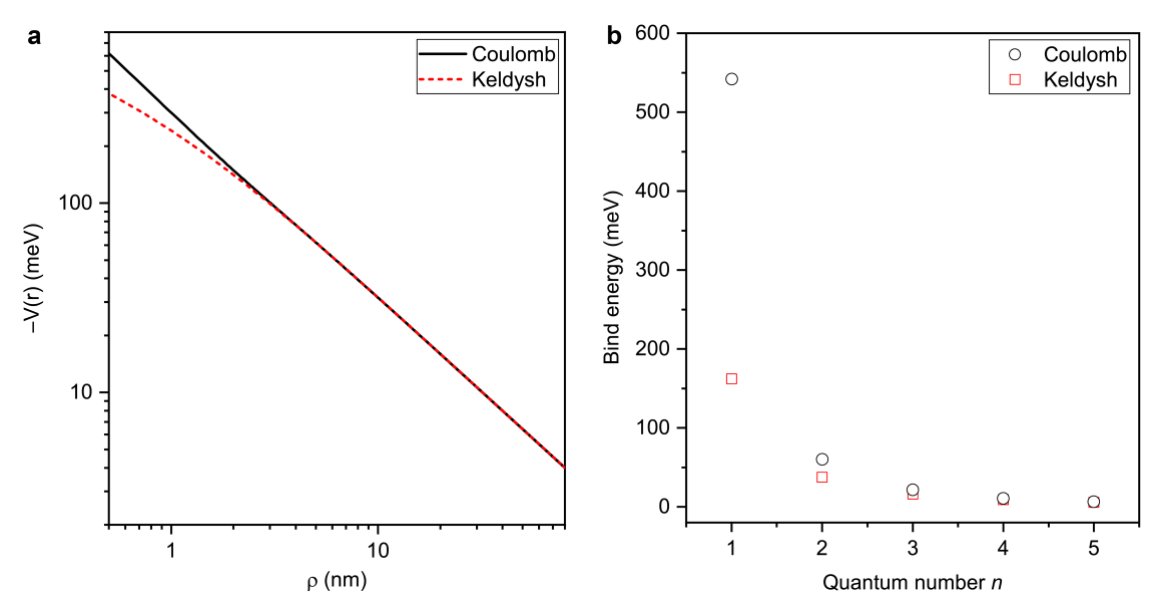
Extended Data Figure 4 | Modeling the 2s exciton Rydberg state. a, Schematic structure of the device geometry. The graphite gates are assumed to be far away from the excitons and are not shown. An electron-hole pair with separation ρ in the sensor layer is separated from the moiré sample (with thickness d_2) by a distance d_1 . The sample and the sensor are both encapsulated in hBN (blue). d_1 and d_2 are set at 0.9 nm and 0.6 nm, respectively, to represent the realistic device geometry. b, c, Dependence of the screened electron-hole Coulomb potential $-V(\rho)$ (b) and the 2s exciton wavefunction $\Psi_{ns}(\rho)$ (c) on the electron-hole separation ρ for representative ratios of the dielectric constants $\frac{\varepsilon}{\varepsilon_{BN}}$. d, e, Dependence of the 2s Bohr radius (d) and the 2s binding energy on the ratio $\frac{\varepsilon}{\varepsilon_{BN}}$. The black line is a power-law fit to the result for $\frac{\varepsilon}{\varepsilon_{BN}}$ between 10^2 and 10^4 . f, Dependence of the 2s binding energy on the 2s Bohr radius. The black line is a power-law fit to the result.



Extended Data Figure 5 | Critical exponents for the MITs. a, b, The 2s exciton spectral weight as a function of the electric field at $\nu=3$ (a) and 7/3 (b). The solid lines are the smoothed data using the Savitzky-Golay algorithm with a window of 80 mV/nm. The arrows denote the chosen critical electric fields E_c of the MITs; the value of E_c cannot be determined accurately in our experiment. c, d, Dependence of the normalized dielectric constant $\bar{\varepsilon}$ on the reduced electric field $E-E_c$ in log-log scale for $\nu=3$ (c) and 7/3 (d). The solid lines are linear fits to the data near E_c over a limited range of $E-E_c$ in order to estimate the value of the critical exponent γ , which varies from 1.6 to 2.2 for $\nu=3$ and from 1.2 to 1.8 for $\nu=7/3$. Different colors correspond to different chosen values of E_c .



Extended Data Figure 6 | Band alignment in large-twist-angle MoSe₂/WS₂. a, b, The doping density dependent reflectance contrast spectrum of the MoSe₂ (a) and WS₂ (b) intralayer excitons under zero electric field. The gate voltage V_G here only changes the doping density (n). The white dashed lines indicate the onset of electron and hole doping. Charged excitons are only observed in the MoSe₂ layer, consistent with a type-I band alignment in MoSe₂/WS₂ heterobilayers. c,d, The electric-field dependent reflectance contrast spectrum of the MoSe₂ (c) and WS₂ (d) intralayer excitons at a constant electron doping density 3.7×10^{12} cm⁻². The white dashed lines, where the transition from charged exciton to neutral exciton occurs, correspond to the onset of charge transfer between MoSe₂ and WS₂. The corresponding electric field is used to determine the band offsets. e, The determined band alignment in MoSe₂/WS₂ heterobilayers (Methods). Energies are denoted in meV. E_{Mo} and E_W are the optical gaps of MoSe₂ and WS₂, respectively. Δ_C and Δ_V are the conduction and valence band offsets, respectively.



Extended Data Figure 7 | Comparison between the Coulomb and Rytova-Keldysh potential. a, The Coulomb and Rytova-Keldysh potential as a function of the electron-hole distance in a 2D plane (dielectric constant = 4.5). Substantial difference is observed only for distances smaller than the 1s exciton Bohr radius ~ 2 nm. b, The exciton binding energy as a function of the principle quantum number for the Coulomb and the Rytova-Keldysh potentials. Negligible difference is observed for $n \ge 2$.